

Rashba and Weyl spin-orbit coupling in an optical lattice clock

Xiaofan Zhou,^{1,2} Xi-Wang Luo,¹ Gang Chen,^{2,3,*} Suotang Jia,^{2,3} and Chuanwei Zhang^{1,†}

¹*Department of Physics, The University of Texas at Dallas, Richardson, Texas 75080, USA*

²*State Key Laboratory of Quantum Optics and Quantum Optics Devices,
Institute of Laser Spectroscopy, Shanxi University, Taiyuan 030006, China*

³*Collaborative Innovation Center of Extreme Optics,
Shanxi University, Taiyuan, Shanxi 030006, China*

Recent experimental realization of one-dimensional (1D) spin-orbit coupling (SOC) for ultracold alkaline-earth(-like) atoms in optical lattice clocks opens a new avenue for exploring exotic quantum matter because of the strongly suppressed heating of atoms from lasers comparing with alkaline atoms. Here we propose a scheme to realize two-dimensional (2D) Rashba and three-dimensional (3D) Weyl types of SOC in a 3D optical lattice clock and explore their topological phases. With 3D Weyl SOC, the system can support topological phases with various numbers as well as types (I or II) of Weyl points. The spin textures of such topological bands for 2D Rashba and 3D Weyl SOC can be detected using suitably designed spectroscopic sequences. Our proposal may pave the way for the experimental realization of robust topological quantum matters and their exotic quasiparticle excitations in ultracold atomic gases.

Introduction.—Spin-orbit coupling (SOC) plays a key role for many condensed matter phenomena, such as anomalous and spin Hall effects [1], topological insulators and superconductors [2–4], etc. The recent experimental realization of 1D [5–12] and 2D [13–15] SOC in ultracold alkaline atoms provides a highly controllable and disorder-free platform for exploring nontrivial topological physics induced by SOC, such as Majorana fermions with non-Abelian exchange statistics [16–19] and Weyl fermions [20–24] carrying topological monopole charges [25]. However, the experimental observation of these topological phenomena is greatly hindered by the heating of atoms, particularly fermions, originating from the Raman process where lasers couple hyperfine ground states with high-lying excited states. The single-photon detuning for Raman lasers is limited by the fine-structure splitting [5–15] for the generation of SOC, which is usually small for alkaline atoms, yielding large spontaneous emission of photons that heat the atomic gas.

The heating issue may be overcome by choosing atomic species with large fine-structure splitting such as Dy and Er [26, 27] or using alkaline-earth(-like) atoms [28] with long-lived excited states [e.g., the lifetime for ⁸⁷Sr (¹⁷³Yb) is ~ 160 (~ 20) seconds]. For alkaline-earth(-like) atoms, 1D SOC has been theoretically proposed [28] and experimentally realized [29–31] recently through directly coupling the ground ¹S₀ (referred as $|g\rangle$) and excited metastable ³P₀ (referred as $|e\rangle$) clock-states in 1D optical lattice clocks, which does not involve any Raman process. With the recent experimental success in realizing 2D and 3D optical lattice clocks for both Bose and Fermi atoms [32, 33], a natural question is whether 2D and 3D SOC can also be realized without any Raman process.

Here, we address this important question by proposing a scheme for realizing both 2D Rashba and 3D Weyl types of SOC for alkaline-earth(-like) atoms in a 3D op-

tical lattice clock [34] using a simple experimental setup without involving Raman process. The experimental realization of the proposed scheme should pave the way for the eventual experimental generation of stable topological superfluids without heating and the observation of topological Majorana [18, 19] and Weyl fermions [20–22] in ultracold atomic gases. Our main results are:

i) Beside the 3D optical lattice potential generated with magic wavelength lasers, a clock laser that couples two states $|g\rangle$ and $|e\rangle$ is coherently splitted into four beams propagating along different directions (see Fig. 1) and their interference generates the SOC. 3D Weyl (2D Rashba) types of SOC are realized when the wavevectors of the clock laser do (not) possess z -components.

ii) In the presence of 3D Weyl types of SOC, there exists a rich phase diagram containing topological phases with various number of Weyl points as well as a fully gapped 3D Chern insulator phase. The Weyl points can be type-I or type-II [21, 35]. Different Weyl points with opposite topological charges are connected by gapless Fermi arcs on the surface.

iii) Three spectroscopic sequences are proposed to accurately measure the spin textures of the topological bands for 2D Rashba and 3D Weyl SOC using a combination of Rabi spectroscopy and time-of-flight images.

Experimental scheme and theoretical modeling.—Our proposed experimental scheme for generating SOC for alkaline-earth(-like) atomic gases ⁸⁷Sr (¹⁷³Yb) [28–31] is illustrated in Fig. 1. A large magnetic field is applied along the z -direction so that only two nuclear-spin-polarized states ($|g\rangle$ and $|e\rangle$) that form an effective spin-1/2 in ground ¹S₀ and metastable excited ³P₀ manifolds are populated and coupled by a clock laser [see Fig. 1(a)]. The state-independent 3D optical lattice potential $V_{\text{lat}}(\mathbf{r}) = -V_0 [\cos^2(k_L x) + \cos^2(k_L y)] - V_z \cos^2(k_L^z z)$ (the same for $|g\rangle$ and $|e\rangle$) are implemented using six plane-wave lasers [see red arrows in Fig. 1(b)]

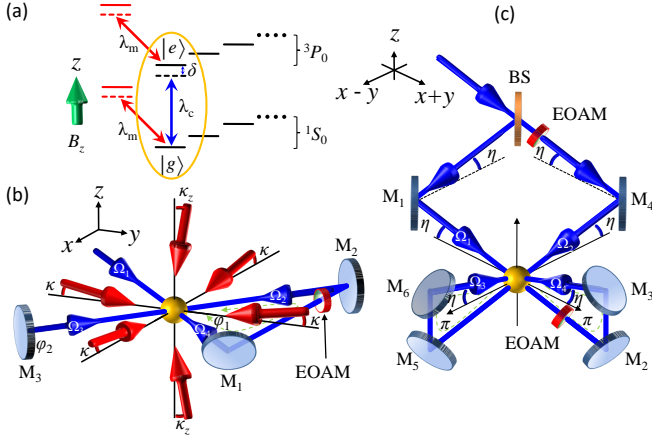


FIG. 1: Schematics of the proposed experimental setup for generating 2D Rashba and 3D Weyl SOC. (a) Optical transitions. With a magnetic field applied along the z -direction, two nuclear-spin-polarized states can be isolated and chosen as two spin states $|g\rangle$ and $|e\rangle$ for the SOC. Blue arrow represents the clock laser transition, with the single-photon detuning δ . Red arrows represent magic wavelength lasers for 3D optical lattices. (b) Laser setup for 2D Rashba SOC. (c) Clock laser setup for 3D Weyl SOC. Optical lattice lasers are the same as (b). Here EOAM represents electro-optic amplitude modulator which is used to turn on/off relevant laser beams for the experimental detection.

with the magic wavelength λ_m (813 nm for ^{87}Sr and 759 nm for ^{173}Yb) [34]. Here $k_L = 2\pi \cos(\kappa)/\lambda_m$ and $k_L^z = 2\pi \cos(\kappa_z)/\lambda_m$ are the wavevectors in the x - y plane and z -direction, with κ and κ_z corresponding laser incident angles.

The two states $|g\rangle$ and $|e\rangle$ are coupled by a clock laser with wavelength λ_c (698 nm for ^{87}Sr and 578 nm for ^{173}Yb). In the rotating frame, the single-particle Hamiltonian can be written as

$$H = \left[\frac{\mathbf{p}^2}{2m} + V_{\text{lat}}(\mathbf{r}) \right] I + m_z \sigma_z + \hbar (M \sigma_+ + \text{H.c.}), \quad (1)$$

where \mathbf{p} is the momentum operator, m is the mass of atoms, $m_z = \hbar \delta$ is the effective Zeeman field determined by the clock laser detuning, and σ_j (I) is the Pauli (identity) matrix on the $\{|g\rangle, |e\rangle\}$ basis. For the generation of 2D and 3D SOC, the spatial distribution of the Rabi coupling of the clock laser is designed to be $M = M_0 e^{-ik_R^z z} [\sin(k_c x) \cos(k_c y) + i \cos(k_c x) \sin(k_c y)]$, which can be realized through suitable interference of the clock laser beams. Figure 1(b) shows the experimental setup for realizing 2D Rashba SOC with $k_R^z = 0$, where the clock laser (linearly polarized along the z -direction) is reflected by three mirrors (M_1 , M_2 and M_3) and propagates along the $(x \pm y)$ -directions in the intersecting area with corresponding Rabi frequencies $\Omega_1 = \Omega_0 e^{ik_c(x+y)}$, $\Omega_2 = \Omega_0 e^{ik_c(x-y) + i\varphi_1}$, $\Omega_3 = \Omega_0 e^{-ik_c(x-y) + i(\varphi_1 + \varphi_2)}$, and $\Omega_4 = \Omega_0 e^{-ik_c(x+y) + i(2\varphi_1 + \varphi_2)}$. Without loss of generality,

we set Ω_0 to be real because its overall phase originating from the initial phase of the incident laser can be gauged out without affecting the SOC. $k_c = 2\pi/(\sqrt{2}\lambda_c)$, φ_1 (φ_2) is the phase acquired by the beam when it propagates along the optical path from the atom cloud over mirrors $M_{1,2}$ (M_3) then back to the atom cloud. The total Rabi coupling strength $M = \sum_{\Lambda=1}^4 \Omega_{\Lambda}$ has above designed form by choosing $\varphi_1 = 0 \pmod{2\pi}$, $\varphi_2 = \pi \pmod{2\pi}$, and $M_0 = 2\sqrt{2}\Omega_0$. We choose $k_c = k_L$ for the generation of desired 2D Rashba SOC, yielding $\cos(\kappa) = \lambda_m/(\sqrt{2}\lambda_c) \approx 0.8$ for ^{87}Sr (0.9 for ^{173}Yb).

The generation of 3D SOC requires the phase factor $e^{-ik_R^z z}$ in the Rabi coupling M , which can be realized by tilting the four clock laser beams Ω_{Λ} by an angle η with respect to the x - y plane with $k_R^z = 2\pi \sin(\eta)/\lambda_c$. In the x - y plane, $k_L = k_c = 2\pi \cos(\eta)/(\sqrt{2}\lambda_c)$ yields $\cos(\kappa)/\cos(\eta) = \lambda_m/(\sqrt{2}\lambda_c)$. Such 3D Ω_{Λ} can be realized with a similar optical setup with mirrors and a beam splitter [see Fig. 1(c)]. Note that the electric field of the clock laser has a component in the x - y plane, which, however, does not induce the transition to other nuclear-spin states due to the large Zeeman splitting [see Fig. 1(a)]. Such Rabi coupling between two pseudospin states does not involve the Raman process that requires a small detuning to unstable high excited states and induces large spontaneous emission of photons. Furthermore, the Raman transition between different Zeeman states requires careful design of laser polarizations of Raman beams, which is not necessary for the Rabi transition here, yielding a simpler optical setup.

With typical optical lattice potential depths, atoms are confined in the lowest band of the lattice and tight-binding approximation can be applied. It is straightforward to derive corresponding tight-binding lattice model for the Hamiltonian Eq. (1), which yields an effective Hamiltonian [36]

$$\mathcal{H}_E = \sum_{\mathbf{k}, s, s'} \hat{c}_{\mathbf{k}, s}^{\dagger} \mathbf{H}_{\mathbf{k}} \hat{c}_{\mathbf{k}, s'}, \quad (2)$$

where $s = (g, e)$, and $\hat{c}_{\mathbf{k}, s}^{\dagger}$ ($\hat{c}_{\mathbf{k}, s}$) is the creation (annihilation) operator for state s at momentum $\mathbf{k} = (k_x, k_y, k_z)$. $\mathbf{H}_{\mathbf{k}} = h_{0\mathbf{k}} I + \mathbf{h}_{\mathbf{k}} \cdot \boldsymbol{\sigma}$, where $h_{0\mathbf{k}} = -2t_z \cos(k_z a_z) \cos(\phi/2)$, $h_{x\mathbf{k}} = -2t_{s0} \sin(k_y a)$, $h_{y\mathbf{k}} = -2t_{s0} \sin(k_x a)$, and $h_{z\mathbf{k}} = m_z - 2t \cos(k_x a) - 2t \cos(k_y a) + 2t_z \sin(k_z a_z) \sin(\phi/2)$. t_z is the hopping parameter along the z -direction, and $\phi = \pi k_R^z / k_L^z$. a_z and a are optical lattice constants in the z -direction and x - y plane, respectively. t and t_{s0} are spin-preserved and spin-flipped hopping parameters in the x - y plane, and the latter is induced by the Rabi coupling M of the clock laser. The energy spectrum of the Hamiltonian can be easily obtained through diagonalizing the $\mathbf{H}_{\mathbf{k}}$, yielding $E_{\mathbf{k}} = h_{0\mathbf{k}} \pm |\mathbf{h}_{\mathbf{k}}|$.

When $k_R^z = 0$ (*i.e.*, clock laser is in the x - y plane), $\phi = 0$ and $h_{z\mathbf{k}} = m_z - 2t \cos(k_x a) - 2t \cos(k_y a)$, therefore there is no coupling between momentum k_z and spin, leaving 2D Rashba type of SOC in the x - y plane in the

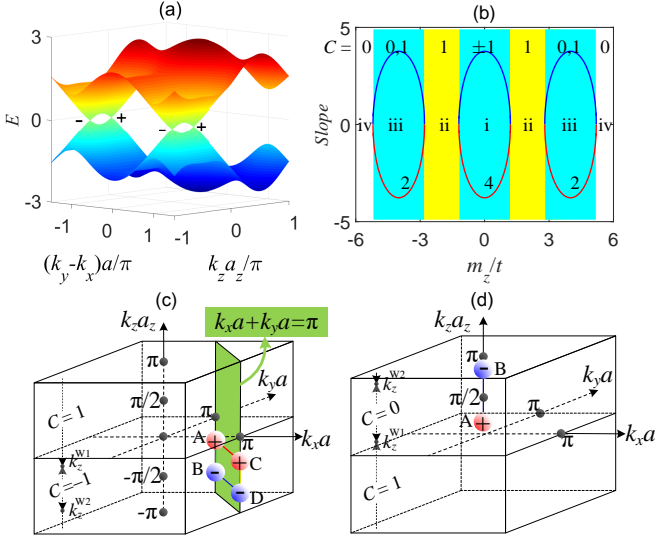


FIG. 2: Topological phases in 3D with $\phi = \pi$. In all panels $t_{so}/t = 0.6$, $t_z/t = 0.6$. (a) Energy spectrum $E_{\mathbf{k}}$ with four Weyl points in the $k_x a + k_y a = \pi$ plane, with their topological charges ± 1 . $m_z/t = 1$. (b) The phase diagram with different m_z . (2, 4, 2) indicate the number of Weyl points. Blue and red lines represent two slopes $\pm 2t_z \cos(\gamma)$ of the energy dispersions along the k_z -direction near a Weyl point. The Chern number C is defined in the k_x - k_y plane for fixed $k_z a_z$. (c) and (d) Positions and charges of Weyl points for cases *i*) and *iii*) respectively.

Hamiltonian Eq. (2). In this case, the single particle physics is described by a topological phase transition between a trivial insulator for $|m_z| > 4t$ and a topological insulator for $|m_z| < 4t$, with the phase boundary $|m_z| = 4t$ determined by $|\mathbf{h}_{\mathbf{k}}| = 0$ [14, 37]. Such 2D Rashba SOC not only mixes states $|g\rangle$ and $|e\rangle$, but also lifts the band degeneracy with a single Fermi surface. In the presence of s -wave pairing interaction between two states, the fermionic superfluid pairing supports Majorana fermions inside vortex cores [18, 19], which possess non-Abelian exchange statistics and are a building block for fault-tolerant topological quantum computation [16, 17].

Topological phases with 3D SOC.—When $k_R^z \neq 0$, $\phi = \pi k_R^z/k_L^z \neq 0$, and the Hamiltonian Eq. (2) contains the coupling $2t_z \sin(k_z a_z) \sin(\phi/2) \sigma_z$ along the k_z -direction. Hereafter we consider only $t > t_z$ and the topological phases for $t \leq t_z$ can be discussed similarly and are presented in the supplementary material [36]. We first consider $\phi = \pi$ (i.e., $k_R^z = k_L^z$), which leads to $h_{0\mathbf{k}} = 0$. From the energy dispersion $E_{\mathbf{k}} = \pm |\mathbf{h}_{\mathbf{k}}|$, we see the spectrum is gapless only when $|\mathbf{h}_{\mathbf{k}}| = 0$, with $h_{x\mathbf{k}} = h_{y\mathbf{k}} = 0$ occurring at $k_x a, k_y a = 0$ or π . At $(k_x a, k_y a) = (0, \pi)$ or $(\pi, 0)$, $h_{z\mathbf{k}} = m_z + 2t_z \sin(k_z a_z)$ becomes zero in the region $|m_z| \leq 2t_z$ at $k_z a_z = \gamma$ or $-\pi - \gamma$ with $\gamma = \arcsin\left[\frac{-m_z}{2t_z}\right]$. While at $(k_x a, k_y a) = (0, 0)$ or

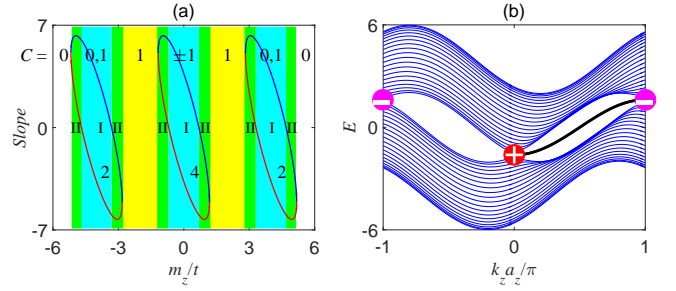


FIG. 3: Type-I and type-II Weyl points for $\phi \neq \pi$. (a) Phase diagram. The notations and parameters are the same as those in Fig. 2(b) except $\phi = 2\pi/5$. I and II indicate the types of the Weyl points. Two slopes are $\nu_0 \pm \nu_z$. (b) Energy spectrum $E_{\mathbf{k}}$ under open boundary condition along the x -direction with $\phi = 2\pi/5$ and $m_z/t = 0.0$. Black line represent the surface state connecting two Weyl points.

(π, π) , $h_{z\mathbf{k}} = m_z \mp 4t + 2t_z \sin(k_z a_z)$ becomes zero only in the region $4t - 2t_z \leq \pm m_z \leq 4t + 2t_z$ at $k_z a_z = \zeta$ or $\pi - \zeta$ with $\zeta = \arcsin\left[\frac{\pm 4t - m_z}{2t_z}\right]$, where the top and bottom signs are for $(0, 0)$ and (π, π) respectively. Outside these two regions ($2t_z < |m_z| < 4t - 2t_z$ and $|m_z| > 4t + 2t_z$), the spectrum is fully gapped.

Each band gap closing point with $E_{\mathbf{k}} = 0$ represents a Weyl point [see Fig. 2(a)], whose topological charge can be determined by Chern number $C = \frac{1}{2\pi} \oint_S B(\mathbf{k}) dS$ of the lowest energy band. Here S is a surface enclosing the Weyl point, and $B(\mathbf{k}) = i \langle \nabla_{\mathbf{k}} \Psi(\mathbf{k}) \times \nabla_{\mathbf{k}} \Psi(\mathbf{k}) \rangle$ is the Berry curvature [1] with $\Psi(\mathbf{k})$ the lower band wavefunction. Based on above gap closing conditions, there exist four different phases for $t_z < t$ in different m_z regions [see Fig. 2(b)]. *i*) $|m_z| \leq 2t_z$: four Weyl points at $\mathbf{k}^W = (k_x a, k_y a, k_z a_z) = (0, \pi, \gamma), (0, \pi, -\pi - \gamma), (\pi, 0, \gamma)$ and $(\pi, 0, -\pi - \gamma)$ with different topological charges [see Fig. 2(c)]. For instance, around $\mathbf{k}^W = (0, \pi, \gamma)$, $\mathbf{h}_{\mathbf{k}} \approx 2t_{so} a (\bar{k}_x \sigma_x - \bar{k}_y \sigma_y) + 2t_z a_z \cos(\gamma) \bar{k}_z \sigma_z$ with the linear dispersion; *ii*) $2t_z < |m_z| < 4t - 2t_z$: a fully gapped topological phase with Chern number $C = 1$ in the k_x - k_y plane for any fixed k_z , corresponding to a stacking 2D Chern insulator; *iii*) $4t - 2t_z \leq \pm m_z \leq 4t + 2t_z$: two Weyl points at $\mathbf{k}^W = (0, 0, \zeta)$ and $(0, 0, \pi - \zeta)$ for $m_z > 0$ [see Fig. 2(d)] or (π, π, ζ) and $(\pi, \pi, \pi - \zeta)$ for $m_z < 0$; *iv*) $|m_z| > 4t + 2t_z$: trivial insulator phase.

For a general $\phi \neq \pi$, there is a nonzero $h_{0\mathbf{k}} = -2t_z \cos(k_z a_z) \cos(\phi/2)$ and t_z in $h_{z\mathbf{k}}$ is also replaced by $t_z \sin(\phi/2)$. $h_{0\mathbf{k}}$ does not change the eigenstates of the Hamiltonian Eq. (2), therefore the phase boundaries between above four cases are only changed by the replacement $t_z \rightarrow t_z \sin(\phi/2)$. However, nonzero $h_{0\mathbf{k}}$ rotates the slopes of the linear dispersions near the Weyl point such that two slopes along the k_z -direction may have the same sign in certain parameter region, which correspond to type-II Weyl points (the traditional one

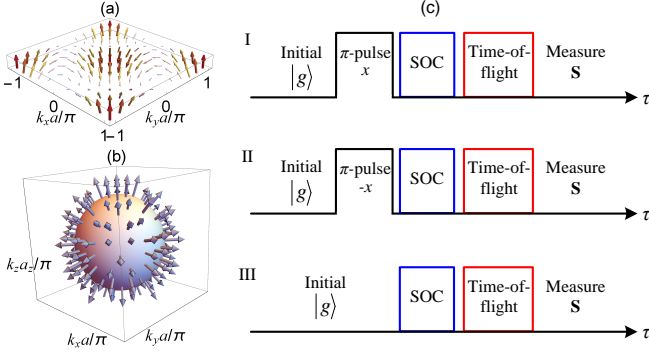


FIG. 4: Detection of spin textures. (a) Spin textures in the k_x - k_y plane with 2D Rashba SOC. $t_{\text{so}}/t = 0.6$, $m_z/t = 0$. (b) Spin textures around a Weyl point with +1 topological charge (the arrows are rotated 90° along the z -axis for better illustration). $t_{\text{so}}/t = 0.6$, $t_z/t = 0.6$, $m_z/t = 0$, and $\phi = \pi$. (c) Three spectroscopic sequences I, II and III for the detection of spin parameters $\theta_{\mathbf{k}}$ and $\varphi_{\mathbf{k}}$.

with opposite signs of slopes is called type-I). For instance, around the Weyl point $\mathbf{k}^W = (0, \pi, \gamma)$ for the case $i) |m_z| \leq 2t_z \sin(\phi/2)$, the Hamiltonian can be expanded as $\mathbf{h}_{\mathbf{k}} = \nu_0 \bar{k}_z + 2t_{\text{so}} a (\bar{k}_x \sigma_x - \bar{k}_y \sigma_y) + \nu_z \bar{k}_z \sigma_z$ with $\nu_0 = 2t_z a_z \sin(\gamma) \cos(\phi/2)$, $\nu_z = 2t_z a_z \cos(\gamma) \sin(\phi/2)$, and $\gamma = \arcsin \left[\frac{-m_z}{2t_z \sin(\phi/2)} \right]$. The Lifshitz transition [38] between type-I and type-II occurs at $|\nu_0| = |\nu_z|$ [i.e., $|m_z^c| = 2t_z \sin^2(\phi/2)$]. The phase diagram and corresponding types of Weyl points are shown in Fig. 3(a). Finally, because Weyl points do not stay at $E_{\mathbf{k}} = 0$ plane due to nonzero $h_{0\mathbf{k}}$, the surface states are now embedded in the bulk spectrum [see Fig. 3(b)], instead of the straight Fermi arc at $E_{\mathbf{k}} = 0$ connecting two Weyl points with opposite charges for $\phi = \pi$.

Experimental detection of spin textures.—The topological properties of 2D Rashba and 3D Weyl SOC can be characterized by their spin textures in the momentum space, which are shown in Figs. 4(a) and 4(b). These spin textures are determined by the effective field $\mathbf{h}_{\mathbf{k}}$ in the Hamiltonian Eq. (2) and can be parameterized by angles $\theta_{\mathbf{k}} = \arctan \left(\sqrt{h_{x\mathbf{k}}^2 + h_{y\mathbf{k}}^2} / h_{z\mathbf{k}} \right)$ and $\varphi_{\mathbf{k}} = \arctan(h_{y\mathbf{k}}/h_{x\mathbf{k}})$ at each momentum \mathbf{k} . Here we propose a spectroscopic procedure [36] to determine the parameter $(\theta_{\mathbf{k}}, \varphi_{\mathbf{k}})$ by measuring the time dynamics of spin polarization $\langle \mathbf{S}(\mathbf{k}) \rangle$, which are obtained through a combination of momentum-resolved Rabi spectroscopy [28] and time-of-flight imaging. Three spectroscopic sequences, as shown in Fig. 4(c), are used to eliminate various side effects and obtain accurate results. In all sequences, atoms are initially prepared in state $|g\rangle$ at half filling without SOC.

I): First a π -pulse along σ_x is applied using the clock laser, which excites atoms from $|g\rangle$ to $|e\rangle$ with a momentum transfer $\mathbf{Q} = (k_c, k_c, k_R^z)$ that is the same as that of

the SOC. Therefore the π -pulse couples two pseudospin states with the same quasi-momentum $|g, \mathbf{k}\rangle \leftrightarrow |e, \mathbf{k}\rangle$. Such a π -pulse can be implemented using one of the four SOC beams, with the other three turned off by electro-optic amplitude modulators (EOAM) [39], as shown in Figs. 1(b) and 1(c). In the quasi-momentum space, the tight-binding dispersion of state $|e\rangle$ is inverted with respect to state $|g\rangle$, therefore the energy splitting at different \mathbf{k} is different. With suitably chosen clock laser frequency, we can selectively excite atoms at certain \mathbf{k}^* using a weak pulse (compared to the tight-binding band width), such that only atoms near \mathbf{k}^* are excited and atoms away from \mathbf{k}^* are off-resonance and remain in state $|g\rangle$. Notice that the resonance momentum \mathbf{k}^* is not single valued, which form a circle in 2D and a surface (spherical for type-I or ellipsoid-like for type-II Weyl points) in 3D. We can select a different \mathbf{k}^* by slightly changing the frequency of the π -pulse, thus cover the whole momentum space.

After the π -pulse, we turn on the 2D (3D) SOC and the system evolves under the Hamiltonian Eq. (2) for an interval τ . Then the SOC and lattice potentials are turned off and the time-of-flight images are taken to determine the spin polarization $\langle \mathbf{S}(\mathbf{k}) \rangle$ at each \mathbf{k} on the \mathbf{k}^* ring or surface as a function of τ . Suitable spin rotations using pulses along different spin axis with clock lasers may be needed before the time-of-flight to measure different components of $\langle \mathbf{S}(\mathbf{k}) \rangle$.

II): Sequence II is the same as I except that the π -pulse is along $-\sigma_x$, which is used to eliminate effects caused by atoms near resonance momenta \mathbf{k}^* that may be partially pumped to $|e\rangle$ (with amplitude $f_{\mathbf{k}}$). Because of the partial excitation amplitude $f_{\mathbf{k}}$, the spin polarizations $\langle \mathbf{S}(\mathbf{k}) \rangle_{\text{I,II}}$ obtained from sequences I or II become complicated functionals of $f_{\mathbf{k}}, \theta_{\mathbf{k}}, \varphi_{\mathbf{k}}, \tau$. However, $f_{\mathbf{k}}$ appears as a simple overall factor in their average [36]

$$\frac{\langle \mathbf{S}(\mathbf{k}) \rangle_{\text{I}} + \langle \mathbf{S}(\mathbf{k}) \rangle_{\text{II}}}{2} = \left(\frac{1}{2} - |f_{\mathbf{k}}|^2 \right) \mathbf{T}(\theta_{\mathbf{k}}, \varphi_{\mathbf{k}}, \tau), \quad (3)$$

with $\mathbf{T}(\theta_{\mathbf{k}}, \varphi_{\mathbf{k}}, \tau)$ a simple dynamical function which can be used to determine $\theta_{\mathbf{k}}, \varphi_{\mathbf{k}}$.

III): Sequence III is the same as I without the π -pulse, which is used to filter the dynamics of the excited atoms from the remaining $|g\rangle$ atoms by canceling the $1/2$ in Eq. (3). As a result, signals for atoms with momenta far away from \mathbf{k}^* are eliminated because $f_{\mathbf{k}}$ is nonzero only in a narrow interval around \mathbf{k}^* ring or surface. This process isolates the dynamics of atoms near \mathbf{k}^* , and we can then replace $\theta_{\mathbf{k}}, \varphi_{\mathbf{k}}$ by $\theta_{\mathbf{k}^*}, \varphi_{\mathbf{k}^*}$ in Eq. (3), from which we can extract their values [36].

Conclusions.—In summary, we proposed a scheme for realizing and detecting 2D Rashba and 3D Weyl types of SOC for alkaline-earth(-like) atoms in optical lattice clocks without involving Raman process, therefore the heating of atoms due to lasers is strongly suppressed. In combination with s -wave scattering interaction between

atoms, our scheme provides a powerful platform for realizing stable topological superfluids and observing associated topological excitations, such as Majorana fermions, which may have potential applications in fault-tolerant topological quantum computation.

Acknowledgements: X. Z., G. C., and S. J. are supported by National Key R&D Program of China under Grants No. 2017YFA0304203; the NSFC under Grants No. 11434007 and No. 11674200; the PCSIRT under Grant No. IRT13076; SFSSSP; OYTPSP; and 1331KYC. X. L. and C. Z. are supported by AFOSR (FA9550-16-1-0387), NSF (PHY-1505496), and ARO (W911NF-17-1-0128).

* Electronic address: chengang971@163.com

† Electronic address: chuanwei.zhang@utdallas.edu

- [1] D. Xiao, M.-C. Chang, and Q. Niu, Berry phases effects on electronic properties, *Rev. Mod. Phys.* **82**, 1959 (2010).
- [2] M. Z. Hasan and C. L. Kane, Topological insulators, *Rev. Mod. Phys.* **82**, 3045 (2010).
- [3] X.-L. Qi and S.-C. Zhang, Topological insulators and superconductors, *Rev. Mod. Phys.* **83**, 1057 (2011).
- [4] J. E. Moore, The birth of topological insulators, *Nature (London)* **464**, 194 (2010).
- [5] Y.-J. Lin, K. Jiménez-García, and I. B. Spielman, Spin-orbit-coupled Bose-Einstein condensates, *Nature (London)* **471**, 83 (2011).
- [6] Z. Fu, P. Wang, S. Chai, L. Huang, and J. Zhang, Bose-Einstein condensate in a light-induced vector gauge potential using the 1064 nm optical dipole trap lasers, *Phys. Rev. A* **84**, 043609 (2011).
- [7] J.-Y. Zhang, S.-C. Ji, Z. Chen, L. Zhang, Z.-D. Du, B. Yan, G.-S. Pan, B. Zhao, Y.-J. Deng, H. Zhai, S. Chen, and J.-W. Pan, Collective dipole oscillations of a spin-orbit coupled Bose-Einstein condensate, *Phys. Rev. Lett.* **109**, 115301 (2012).
- [8] C. Qu, C. Hamner, M. Gong, C. Zhang, and P. Engels, Observation of Zitterbewegung in a spin-orbit coupled Bose-Einstein condensates, *Phys. Rev. A* **88**, 021604(R) (2013).
- [9] A. J. Olson, S.-J. Wang, R. J. Niffenegger, C. -H. Li, C. H. Greene, and Y. P. Chen, Tunable Landau-Zener transitions in a spin-orbit-coupled Bose-Einstein condensate, *Phys. Rev. A* **90**, 013616 (2014).
- [10] P. Wang, Z. Yu, Z. Fu, J. Miao, L. Huang, S. Chai, H. Zhai, and J. Zhang, Spin-orbit coupled degenerate Fermi gases, *Phys. Rev. Lett.* **109**, 095301 (2012).
- [11] L. W. Cheuk, A. T. Sommer, Z. Hadzibabic, T. Yefsah, W. S. Bakr, and M. W. Zwierlein, Spin-injection spectroscopy of a spin-orbit coupled Fermi gas, *Phys. Rev. Lett.* **109**, 095302 (2012).
- [12] R. A. Williams, M. C. Beeler, L. J. LeBlanc, and I. B. Spielman, Raman-induced interactions in a single-component Fermi gas near an *s*-wave Feshbach resonance, *Phys. Rev. Lett.* **111**, 095301 (2013).
- [13] L. Huang, Z. Meng, P. Wang, P. Peng, S.-L. Zhang, L. Chen, D. Li, Q. Zhou, and J. Zhang, Experimental realization of two-dimensional synthetic spin-orbit coupling in ultracold Fermi gases, *Nat. Phys.* **12**, 540 (2016).
- [14] Z. Wu, L. Zhang, W. Sun, X.-T. Xu, B.-Z. Wang, S.-C. Ji, Y. Deng, S. Chen, X.-J. Liu, and J.-W. Pan, Realization of two-dimensional spin-orbit coupling for Bose-Einstein condensates, *Science* **354**, 83 (2016).
- [15] Z. Meng, L. Huang, P. Peng, D. Li, L. Chen, Y. Xu, C. Zhang, P. Wang, and J. Zhang, Experimental observation of a topological band gap opening in ultracold Fermi gases with two-dimensional spin-orbit coupling, *Phys. Rev. Lett.* **117**, 235304 (2016).
- [16] C. Nayak, S. H. Simon, A. Stern, M. Freedman, and S. D. Sarma, Non-Abelian anyons and topological quantum computation, *Rev. Mod. Phys.* **80**, 1083 (2008).
- [17] F. Wilczek, Majorana returns, *Nat. Phys.* **5**, 614 (2009).
- [18] C. Zhang, S. Tewari, R. M. Lutchyn, and S. Das Sarma, $p_x + ip_y$ superfluid from *s*-wave interactions of fermionic cold atoms, *Phys. Rev. Lett.* **101**, 160401 (2008).
- [19] M. Gong, G. Chen, S. Jia, and C. Zhang, Searching for Majorana fermions in 2D spin-orbit coupled Fermi superfluids at finite temperature, *Phys. Rev. Lett.* **109**, 105302 (2012).
- [20] M. Gong, S. Tewari, and C. Zhang, BCS-BEC crossover and topological phase transition in 3D spin-orbit coupled degenerate Fermi gases, *Phys. Rev. Lett.* **107**, 195303 (2011).
- [21] Y. Xu, F. Zhang, and C. Zhang, Structured Weyl points in spin-orbit coupled fermionic superfluids, *Phys. Rev. Lett.* **115**, 265304 (2015).
- [22] Y. Xu and L.-M. Duan, Type-II Weyl points in three-dimensional cold-atom optical lattices, *Phys. Rev. A* **94**, 053619 (2016).
- [23] T. Dubček, C. J. Kennedy, L. Lu, W. Ketterle, M. Soljačić, and H. Buljan, Weyl points in three-dimensional optical lattices: synthetic magnetic monopoles in momentum space, *Phys. Rev. Lett.* **114**, 225301 (2015).
- [24] B.-Z. Wang, Y.-H. Lu, W. Sun, S. Chen, Y. Deng, and X.-J. Liu, Dirac, Rashba and Weyl type spin-orbit couplings: toward experimental realization in ultracold atoms, *Phys. Rev. A* **97**, 011605 (2018).
- [25] G. E. Volovik, *The universe in a helium droplet* (Clarendon Press, Oxford, 2003).
- [26] X. Cui, B. Lian, T.-L. Ho, B. L. Lev, and H. Zhai, Synthetic gauge field with highly magnetic lanthanide atoms, *Phys. Rev. A* **88**, 011601 (2013).
- [27] N. Q. Burdick, Y. Tang, and B. L. Lev, Long-lived spin-orbit-coupled degenerate dipolar Fermi gas, *Phys. Rev. X* **6**, 031022 (2016).
- [28] M. L. Wall, A. P. Koller, S. Li, X. Zhang, N. R. Cooper, J. Ye, and A. M. Rey, Synthetic spin-orbit coupling in an optical lattice clock, *Phys. Rev. Lett.* **116**, 035301 (2016).
- [29] L. F. Livi, G. Cappellini, M. Diem, L. Franchi, C. Clivati, M. Frittelli, F. Levi, D. Calonico, J. Catani, M. Inguscio, and L. Fallani, Synthetic dimensions and spin-orbit coupling with an optical clock transition, *Phys. Rev. Lett.* **117**, 220401 (2016).
- [30] S. Kolkowitz, S. L. Bromley, T. Bothwell, M. L. Wall, G. E. Marti, A. P. Koller, X. Zhang, A. M. Rey, and J. Ye, Spin-orbit-coupled fermions in an optical lattice clock, *Nature (London)* **542**, 66 (2017).
- [31] S. L. Bromley, S. Kolkowitz, T. Bothwell, D. Kedar, A. Safavi-Naini, M.L. Wall, C. Salomon, A.M. Rey, and J. Ye, Dynamics of interacting fermions under spin-orbit coupling in an optical lattice clock, *Nat. Phys.* **14**, 399

- (2018).
- [32] T. Akatsuka, M. Takamoto, and H. Katori, Three-dimensional optical lattice clock with bosonic ^{88}Sr atoms, *Phys. Rev. A* **81**, 023402 (2010).
- [33] S. L. Campbell, R. B. Hutson, G. E. Marti, A. Goban, N. Darkwah Oppong, R. L. McNally, L. Sonderhouse, J. M. Robinson, W. Zhang, B. J. Bloom, and J. Ye, A Fermi-degenerate three-dimensional optical lattice clock, *Science* **358**, 90 (2017).
- [34] A. D. Ludlow, M. M. Boyd, J. Ye, E. Peik, and P. O. Schmidt, Optical atomic clocks, *Rev. Mod. Phys.* **87**, 637 (2015).
- [35] A. A. Soluyanov, D. Gresch, Z. Wang, Q. Wu, M. Troyer, X. Dai, and B. A. Bernevig, Type-II Weyl semimetals, *Nature (London)* **527**, 495 (2015).
- [36] See Supplemental Materials, for the derivation of the tight-binding Hamiltonian, the phase diagram for $t \leq t_z$, and some details of the detection scheme for spin textures.
- [37] X.-J. Liu, K. T. Law, and T. K. Ng, Realization of 2D spin-orbit interaction and exotic topological orders in cold atoms, *Phys. Rev. Lett.* **112**, 086401 (2014).
- [38] I. M. Lifshitz, Anomalies of electron characteristics of a metal in the high pressure region, *Sov. Phys. JETP* **11**, 1130 (1960).
- [39] A. Yariv and P. Yeh, *Photonics: Optical Electronics in Modern Communications* (Oxford University Press, Oxford, 2007).

Supplementary Materials

In this supplemental materials we provide the derivation of the tight-binding Hamiltonian, the phase diagram for $t \leq t_z$, and some details of the detection scheme for spin textures.

A. Tight-binding Hamiltonian

After the single-band approximation and the unitary transformation $U = e^{-ik_{\text{R}}^z z/2} |g\rangle\langle g| + e^{ik_{\text{R}}^z z/2} |e\rangle\langle e|$, we obtain the tight-binding Hamiltonian from Eq. (1) in the main text, which can be written as

$$\begin{aligned}
 \mathcal{H}_{\text{TI}} = & -t \sum_{\langle \vec{j}, \vec{j}' \rangle} \hat{c}_{\vec{j}s}^\dagger \hat{c}_{\vec{j}'s} + m_z \sum_{\vec{j}} \left(\hat{n}_{\vec{j}g} - \hat{n}_{\vec{j}e} \right) \\
 & + \sum_{\langle \vec{j}, \vec{j}' \rangle} \left[t_{\text{so}}^{\vec{j}, \vec{j}'} \hat{c}_{\vec{j}}^\dagger \hat{c}_{\vec{j}'e} + \text{H.c.} \right] \\
 & - t_z \sum_{j_z} \left(e^{i\phi \xi_s / 2} \hat{c}_{j_z s}^\dagger \hat{c}_{j_z + 1s} + \text{H.c.} \right), \tag{4}
 \end{aligned}$$

where $\langle \rangle$ denotes the sum over nearest-neighbor sites with x - y plane lattice-site index $\vec{j} = (j_x, j_y)$, particle number operators $\hat{n}_{\vec{j}s} = \hat{c}_{\vec{j}s}^\dagger \hat{c}_{\vec{j}s}$, and effective Zeeman field $m_z = \hbar\delta$. t is the spin-preserved hopping amplitude along the x (y)-direction, and $t_{\text{so}}^{\vec{j}, \vec{j}'} = \int d^2r W_g(r - r_j) M W_e(r - r_{j'})$ is the spin-flipped hopping parameter along the x (y)-direction with $W_{g,e}(r - r_j)$ the Wannier function at site j . Notice that the spatial period of M (in both x and y -directions) is twice of the period of the optical lattice. As a result, we have $t_{\text{so}}^{\vec{j}, \vec{j}' \pm \vec{e}_\mu} = \pm(-1)^{j_x + j_y} t_{\text{so}}^\mu$, with $\mu = x, y$. For the aforementioned clock transition M , we have $t_{\text{so}}^x = -it_{\text{so}}^y = t_{\text{so}}$. t and t_{so} can be tuned by changing the amplitude of clock laser's Rabi coupling Ω_0 . The last term in Eq. (4) corresponds to spin conserved hopping along the z -direction, where t_z is the hopping amplitude, $\phi = \pi k_{\text{R}}^z / k_{\text{L}}^z$ is the hopping phase (it can be tuned by the angle between the plane-wave laser pair that forms the z -direction lattice), and $\xi_{g,e} = \pm 1$. Due to the spatial dependence of the SOC, the Hamiltonian of x - y plane have a period $2a$, which can be restore to a by applying the following unitary transformation $\hat{c}_{\vec{j}e} \rightarrow e^{i\pi(x_j + y_j)/a} \hat{c}_{\vec{j}e}$. The Fourier transformation of the Eq. (4) to momentum space yield the momentum effective Hamiltonian Eq. (2) in the main text.

B. Phase diagram for $t \leq t_z$

In the main text, we have discussed the topological phases with 3D SOC for $t > t_z$. For $t \leq t_z$, the physics is similar except that more Weyl points may be found in certain parameter region. For simplicity, here we only consider type-I Weyl points with $\phi = \pi$ (*i.e.*, $h_{0\mathbf{k}} = 0$). As we discussed in the main text, the Weyl points can only occur at $k_x a, k_y a = 0$ or π . For $(k_x a, k_y a) = (0, \pi)$ or $(\pi, 0)$, $\mathbf{h}_{\mathbf{k}}$ becomes zero at $k_z a = \gamma$ or $-\pi - \gamma$ with

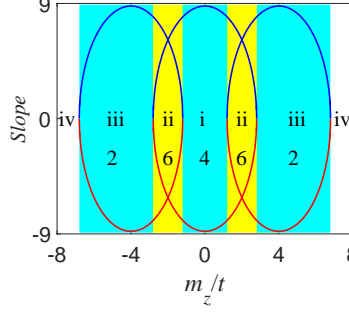


FIG. 5: The phase diagram with Weyl type of SOC. $\phi = \pi$, $t_{\text{so}}/t = 0.6$ and $t_z/t = 1.4$. (2, 6, 4, 6, 2) indicate the number of Weyl points. Blue and red lines represent two slopes $\pm 2t_z \cos(\gamma)$ of the energy dispersions along the k_z direction near a Weyl point.

$\gamma = \arcsin\left[\frac{-m_z}{2t_z}\right]$, leading to 4 Weyl points in the region $|m_z| \leq 2t_z$. Similarly, we have 2 Weyl points in the region $4t - 2t_z \leq m_z < 4t + 2t_z$ ($-4t - 2t_z < m_z \leq -4t + 2t_z$) for $(k_x a, k_y a) = (0, 0)$ [$(k_x a, k_y a) = (\pi, \pi)$]. For $t_z < t$, all these regions are separated without any overlap, therefore we have two fully gapped regions without any Weyl point in $2t_z < |m_z| < 4t - 2t_z$. While for $2t \geq t_z > t$, the region $|m_z| \leq 2t_z$ overlaps with regions $4t - 2t_z \leq m_z < 4t + 2t_z$ and $-4t - 2t_z < m_z \leq -4t + 2t_z$, leading to 6 Weyl points in the regions $4t - 2t_z \leq m_z \leq 2t_z$ and $-2t_z \leq m_z \leq 2t_z - 4t$, as shown in Fig. 5. Moreover, for $t_z > 2t$, all these three regions overlaps, leading to a new region $4t - 2t_z \leq m_z \leq 2t_z - 4t$ with 8 Weyl points.

C. Experimental detection of spin textures using three spectroscopic sequences

Before introducing the details of our detection scheme, we first show how the spin polarization evolves under the SOC Hamiltonian. Consider an atom in an arbitrary initial state $|\psi_0(\mathbf{k})\rangle = \alpha|g_{\mathbf{k}}\rangle + \beta|e_{\mathbf{k}}\rangle$ with momentum \mathbf{k} . Under the SOC Hamiltonian, the state becomes

$$|\psi_{\tau}(\mathbf{k})\rangle = \left[\left(\alpha \frac{\cos \theta_{\mathbf{k}} + 1}{2} + \beta \frac{\sin \theta_{\mathbf{k}}}{2} e^{-i\varphi_{\mathbf{k}}} \right) e^{-iE_{\mathbf{k},-\tau}} + \left(\alpha \frac{1 - \cos \theta_{\mathbf{k}}}{2} - \beta \frac{\sin \theta_{\mathbf{k}}}{2} e^{-i\varphi_{\mathbf{k}}} \right) e^{-iE_{\mathbf{k},+\tau}} \right] |g_{\mathbf{k}}\rangle + \left[\left(\alpha \frac{\sin \theta_{\mathbf{k}}}{2} e^{i\varphi_{\mathbf{k}}} + \beta \frac{1 - \cos \theta_{\mathbf{k}}}{2} \right) e^{-iE_{\mathbf{k},-\tau}} - \left(\alpha \frac{\sin \theta_{\mathbf{k}}}{2} e^{i\varphi_{\mathbf{k}}} - \beta \frac{\cos \theta_{\mathbf{k}} + 1}{2} \right) e^{-iE_{\mathbf{k},+\tau}} \right] |e_{\mathbf{k}}\rangle, \quad (5)$$

after time τ with $E_{\mathbf{k},\pm} = h_{0\mathbf{k}} \pm |\mathbf{h}_{\mathbf{k}}|$.

Due to the Rabi oscillation, the time dynamics of all components' spin polarizations can be characterized as

$$\begin{aligned} \langle S_z \rangle &= P_z(\alpha, \beta, \tau, \mathbf{k}) \\ &= \frac{1}{2} \left(|\alpha|^2 - |\beta|^2 \right) [\cos^2 \theta_{\mathbf{k}} + \sin^2 \theta_{\mathbf{k}} \cos(2|\mathbf{h}_{\mathbf{k}}|\tau)] \\ &\quad + \frac{1}{2} (\alpha\beta^* + \alpha^*\beta) \cos \theta_{\mathbf{k}} \sin \theta_{\mathbf{k}} \cos \varphi_{\mathbf{k}} [1 - \cos(2|\mathbf{h}_{\mathbf{k}}|\tau)] \\ &\quad + (-i) \frac{1}{2} (\alpha\beta^* - \alpha^*\beta) \sin \theta_{\mathbf{k}} \cos \varphi_{\mathbf{k}} \sin(2|\mathbf{h}_{\mathbf{k}}|\tau), \end{aligned} \quad (6)$$

$$\begin{aligned}
\langle S_y \rangle &= P_y(\alpha, \beta, \tau, \mathbf{k}) \\
&= \frac{1}{4}(-i)(\alpha^* \beta - \alpha \beta^*) [\sin^2 \theta_{\mathbf{k}} + \cos^2 \theta_{\mathbf{k}} \cos(2|\mathbf{h}_{\mathbf{k}}| \tau)] \\
&\quad + \frac{1}{2}(|\alpha|^2 - |\beta|^2) \cos \theta_{\mathbf{k}} \sin \theta_{\mathbf{k}} \sin \varphi_{\mathbf{k}} [1 - \cos(2|\mathbf{h}_{\mathbf{k}}| \tau)] \\
&\quad + \frac{1}{4}(-i)(\alpha \beta^* - \alpha^* \beta) \sin^2 \theta_{\mathbf{k}} \cos 2\varphi_{\mathbf{k}} [1 - \cos(2|\mathbf{h}_{\mathbf{k}}| \tau)] \\
&\quad + \frac{1}{4}(\alpha \beta^* + \alpha^* \beta) \sin^2 \theta_{\mathbf{k}} \sin 2\varphi_{\mathbf{k}} [1 - \cos(2|\mathbf{h}_{\mathbf{k}}| \tau)] \\
&\quad + \frac{1}{4}(-i) \alpha^* \beta \cos(2|\mathbf{h}_{\mathbf{k}}| \tau) \\
&\quad + \frac{1}{4} \left[2(|\alpha|^2 - |\beta|^2) \sin \theta_{\mathbf{k}} \cos \varphi_{\mathbf{k}} - 2(\alpha^* \beta + \alpha \beta^*) \cos \theta_{\mathbf{k}} - \alpha \beta^* \right] \sin(2|\mathbf{h}_{\mathbf{k}}| \tau), \tag{7}
\end{aligned}$$

and

$$\begin{aligned}
\langle S_x \rangle &= P_x(\alpha, \beta, \tau, \mathbf{k}) \\
&= \frac{1}{4}(\alpha^* \beta + \alpha \beta^*) [\sin^2 \theta_{\mathbf{k}} + \cos^2 \theta_{\mathbf{k}} \cos(2|\mathbf{h}_{\mathbf{k}}| \tau)] \\
&\quad + \frac{1}{2}(|\alpha|^2 - |\beta|^2) \cos \theta_{\mathbf{k}} \sin \theta_{\mathbf{k}} \cos \varphi_{\mathbf{k}} [1 - \cos(2|\mathbf{h}_{\mathbf{k}}| \tau)] \\
&\quad + \frac{1}{4}(\alpha \beta^* + \alpha^* \beta) \sin^2 \theta_{\mathbf{k}} \cos 2\varphi_{\mathbf{k}} [1 - \cos(2|\mathbf{h}_{\mathbf{k}}| \tau)] \\
&\quad + \frac{1}{4}i(\alpha \beta^* - \alpha^* \beta) \sin^2 \theta_{\mathbf{k}} \sin 2\varphi_{\mathbf{k}} [1 - \cos(2|\mathbf{h}_{\mathbf{k}}| \tau)] \\
&\quad + \frac{1}{4}\alpha^* \beta \cos(2|\mathbf{h}_{\mathbf{k}}| \tau) \\
&\quad + \frac{1}{4} \left[2(|\alpha|^2 - |\beta|^2) \sin \theta_{\mathbf{k}} i \sin \varphi_{\mathbf{k}} - 2(\alpha^* \beta - \alpha \beta^*) \cos \theta_{\mathbf{k}} + \alpha \beta^* \right] i \sin(2|\mathbf{h}_{\mathbf{k}}| \tau). \tag{8}
\end{aligned}$$

These equations show the relations between the angles $(\varphi_{\mathbf{k}}, \theta_{\mathbf{k}})$ and the dynamics of spin polarization. In the following, we show that these relations can be used to determine $(\varphi_{\mathbf{k}}, \theta_{\mathbf{k}})$ through three spectroscopic sequences (I, II and III), as shown in Fig. 4(c) in the main text. In all sequences, atoms are initially prepared in the state $|g\rangle$ at half filling without SOC.

In sequence I, a π -pulse along σ_x is applied using the clock laser to induce the $|g\rangle \rightarrow |e\rangle$ transition at the same quasi-momentum. Such a π -pulse can be implemented using one of the four SOC beams, with the other three turned off by electro-optic amplitude modulators. We can selectively excite atoms at certain \mathbf{k}^* using a weak pulse (compared to the tight-binding band width), such that only atoms near \mathbf{k}^* are excited to $|e\rangle$ and atoms away from \mathbf{k}^* are off-resonance and remain in state $|g\rangle$. Then we turn on the 2D (3D) SOC for an interval τ and let the system evolve under the Hamiltonian Eq. (2) in the main text. Even for a weak pulse, atoms near resonance momenta \mathbf{k}^* may still be partially pumped to $|e\rangle$ (with amplitude $f_{\mathbf{k}}$). Because of the partial excitation amplitude $f_{\mathbf{k}}$, the spin polarization becomes a complex function of $\sqrt{1 - |f_{\mathbf{k}}|^2}, -if_{\mathbf{k}}, \tau, \mathbf{k}$, which is $\langle \mathbf{S}(\mathbf{k}) \rangle_{\text{I}} = \mathbf{P}(\sqrt{1 - |f_{\mathbf{k}}|^2}, -if_{\mathbf{k}}, \tau, \mathbf{k})$.

To eliminate the effects of partial excitation, we introduce sequence II which is the same as I except that the π -pulse is along $-\sigma_x$, leading to the spin polarization $\langle \mathbf{S}(\mathbf{k}) \rangle_{\text{II}} = \mathbf{P}(\sqrt{1 - |f_{\mathbf{k}}|^2}, if_{\mathbf{k}}, \tau, \mathbf{k})$. The average between these two sequences gives a simple form of the spin polarization as

$$\frac{1}{2} [\langle \mathbf{S}(\mathbf{k}) \rangle_{\text{I}} + \langle \mathbf{S}(\mathbf{k}) \rangle_{\text{II}}] = \frac{1}{2} \left(\mathbf{P}(\sqrt{1 - |f_{\mathbf{k}}|^2}, -if_{\mathbf{k}}, \tau, \mathbf{k}) + \mathbf{P}(\sqrt{1 - |f_{\mathbf{k}}|^2}, if_{\mathbf{k}}, \tau, \mathbf{k}) \right) = \left(\frac{1}{2} - |f_{\mathbf{k}}|^2 \right) \mathbf{T}(\theta_{\mathbf{k}}, \varphi_{\mathbf{k}}, \tau). \tag{9}$$

Here \mathbf{T} is given as

$$\begin{aligned}
T_z(\theta_{\mathbf{k}}, \varphi_{\mathbf{k}}, \tau) &= [\cos^2 \theta_{\mathbf{k}} + \sin^2 \theta_{\mathbf{k}} \cos(2|\mathbf{h}_{\mathbf{k}}| \tau)], \\
T_y(\theta_{\mathbf{k}}, \varphi_{\mathbf{k}}, \tau) &= \{\cos \theta_{\mathbf{k}} \sin \theta_{\mathbf{k}} \sin \varphi_{\mathbf{k}} - \Theta \sin[2|\mathbf{h}_{\mathbf{k}}| \tau + \arctan(-\cos \theta_{\mathbf{k}} \tan \varphi_{\mathbf{k}})]\}, \\
T_x(\theta_{\mathbf{k}}, \varphi_{\mathbf{k}}, \tau) &= \left\{ \cos \theta_{\mathbf{k}} \sin \theta_{\mathbf{k}} \cos \varphi_{\mathbf{k}} - \Gamma \sin \left[2|\mathbf{h}_{\mathbf{k}}| \tau + \arctan \left(\frac{\cos \theta_{\mathbf{k}}}{\tan \varphi_{\mathbf{k}}} \right) \right] \right\},
\end{aligned}$$

with $\Theta = \sqrt{(\cos \theta_{|\mathbf{k}|} \sin \theta_{|\mathbf{k}|} \sin \varphi_{|\mathbf{k}|})^2 + (\sin \theta_{|\mathbf{k}|} \cos \varphi_{|\mathbf{k}|})^2}$, and $\Gamma = \sqrt{(\cos \theta_{|\mathbf{k}|} \sin \theta_{|\mathbf{k}|} \cos \varphi_{|\mathbf{k}|})^2 + (\sin \theta_{|\mathbf{k}|} \sin \varphi_{|\mathbf{k}|})^2}$.

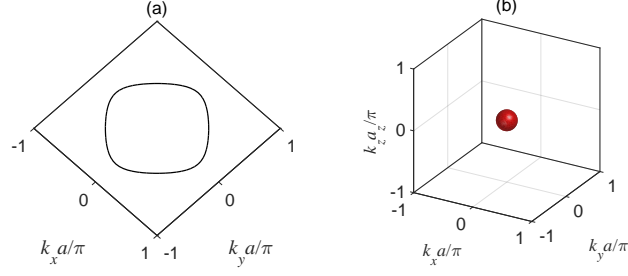


FIG. 6: The resonance momenta \mathbf{k}^* induced by a narrow π -pulse is a circle in 2D (a) and a spherical surface in 3D (b) which surrounds a Weyl point.

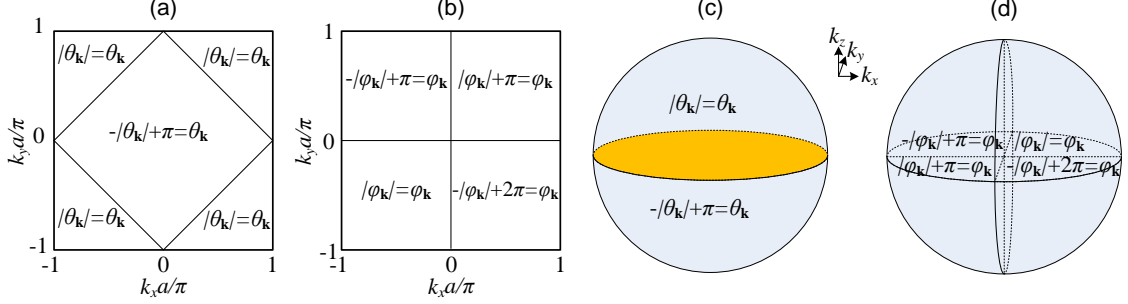


FIG. 7: (a) and (b) The relations between $|\theta_{\mathbf{k}}|$ and $\theta_{\mathbf{k}}$, $|\varphi_{\mathbf{k}}|$ and $\varphi_{\mathbf{k}}$ in 2D. (c) and (d) The relations between $|\theta_{\mathbf{k}}|$ and $\theta_{\mathbf{k}}$, $|\varphi_{\mathbf{k}}|$ and $\varphi_{\mathbf{k}}$ near +1 Weyl points in 3D.

Finally, we use sequence III (which is the same as I without the π -pulse) to filter the dynamics of the excited atoms from the remaining $|g\rangle$ atoms by canceling the $1/2$ in Eq. (9), yielding

$$\frac{1}{2} [\langle \mathbf{S}(\mathbf{k}) \rangle_{\text{I}} + \langle \mathbf{S}(\mathbf{k}) \rangle_{\text{II}}] - \langle \mathbf{S}(\mathbf{k}) \rangle_{\text{III}} = |f_{\mathbf{k}}|^2 \mathbf{T}(\theta_{\mathbf{k}}, \varphi_{\mathbf{k}}, \tau). \quad (10)$$

Without the time-of-flight imaging, the experimentally measured spin-polarization should be summed over the momentum space. We notice that $f_{\mathbf{k}}$ in Eq. (10) is only nonzero around the \mathbf{k}^* ring or surface (see Figs. 6). As a result, time-of-flight images are taken to determine the spin polarization $\langle \mathbf{S} \rangle$ at each \mathbf{k} only on the \mathbf{k}^* ring or surface, rather than the whole momentum space. That is to say, we use the time-of-flight to resolve the azimuthal direction of momentum, and the final observable for a certain point \mathbf{k}^* is

$$\mathbf{O}(\mathbf{k}^*, \tau) = \int |f_{\mathbf{k}}|^2 \mathbf{T}(\theta_{\mathbf{k}}, \varphi_{\mathbf{k}}, \tau) d|\mathbf{k}| \simeq c \mathbf{T}(\theta_{\mathbf{k}^*}, \varphi_{\mathbf{k}^*}, \tau). \quad (11)$$

Here $c = \int |f_{\mathbf{k}}|^2 d|\mathbf{k}|$ is a constant (which is integrated in the radial direction) and we have taken into account that $f_{\mathbf{k}}$ is only nonzero around the \mathbf{k}^* . The angles $|\theta_{\mathbf{k}^*}|$ and $|\varphi_{\mathbf{k}^*}|$ can be inferred from the oscillations of $\mathbf{O}(\mathbf{k}^*, \tau)$:

$$\begin{aligned} 2 \tan^2 \theta_{\mathbf{k}^*} &= \frac{O_z(\mathbf{k}^*, \tau)_{\text{max}} - O_z(\mathbf{k}^*, \tau)_{\text{min}}}{O_z(\mathbf{k}^*, \tau)_{\text{mean}}}, \\ 2 \sqrt{1 + \frac{1}{\cos^2 \theta_{\mathbf{k}^*} \tan^2 \varphi_{\mathbf{k}^*}}} &= \frac{O_y(\mathbf{k}^*, \tau)_{\text{max}} - O_y(\mathbf{k}^*, \tau)_{\text{min}}}{O_y(\mathbf{k}^*, \tau)_{\text{mean}}}, \\ 2 \sqrt{1 + \frac{\tan^2 \varphi_{\mathbf{k}^*}}{\sin^2 \theta_{\mathbf{k}^*}}} &= \frac{O_x(\mathbf{k}^*, \tau)_{\text{max}} - O_x(\mathbf{k}^*, \tau)_{\text{min}}}{O_x(\mathbf{k}^*, \tau)_{\text{mean}}}. \end{aligned} \quad (12)$$

$\theta_{\mathbf{k}^*}$ and $\varphi_{\mathbf{k}^*}$ are determined using the principle of continuity in the momentum space, as shown in Fig. 7. Changing the frequency of the π -pulse, we can obtain $\theta_{\mathbf{k}}$ and $\varphi_{\mathbf{k}}$ in the whole momentum space.